Received: 30 October 2025 | Revised: 11 December 2025 | Accepted: 19 December 2025

DOI: 10.1111/jace.70488

Journal of the American Ceramic Society

RAPID COMMUNICATION

On the asymmetry of soda lime silicate float glass structure and chemistry

Mattia Biesuz[1,2] | **Levent Karacasulu**[1] | **Michele Cassetta**[3,4] | **Mario Barozzi**[5] | **Roberto Canteri**[5] | **Maciej Oskar Liedke**[6] | **Eric Hirschmann**[6] | **Andreas Wagner**[6] | **Sebastiano Mariazzi**[7] | **Gian D. Sorarù**[1,2] | **Vincenzo M. Sglavo**[1,2,8] | **Roberto S. Brusa**[7]

[1]Department of Industrial Engineering, University of Trento, Trento, Italy

[2]INSTM, Firenze, Italy

[3]Department of Earth Science, University of Torino, Torino, Italy

[4]Department of Engineering for Innovation Medicine, University of Verona, Verona, Italy

[5]Fondazione Bruno Kessler, MicroNanoFacility Unit, Trento, Italy

[6]Institute of Radiation Physics, Helmholtz-Zentrum Dresden - Rossendorf, Dresden, Germany

[7]Department of Physics, University of Trento, Povo, Trento, Italy

[8]Istituto di Fotonica e Nanotecnologie, Consiglio Nazionale delle Ricerche, Trento, Italy

Correspondence
Mattia Biesuz, Department of Industrial Engineering, University of Trento, Via Sommarive 9, 38123, Trento, Italy.
Email: mattia.biesuz@unitn.it

Abstract

Soda lime silicate glass produced by the float process is among the materials with the largest use worldwide. The manufacturing process introduces an asymmetry in the glass sheets that causes well-known modifications in terms of properties between the so-called "air side" and "tin side". Nevertheless, not much is known about the structural changes induced by the diffusing tin ions in the network. In the present work, we show that surprisingly, the short range of the tin side is akin to that of the bulk, while the network connectivity in the air side vicinity is enhanced with a larger concentration of bridging oxygens. This correlates with a partial depletion of modifiers from the air side as detected by secondary ion mass spectrometry. On the other hand, the incorporation of tin markedly changes the medium range. In fact, the tin side is characterized by: (i) longer correlation distances, (ii) a more homogeneous structure depicted by a more reduced splitting of the medium frequency Raman features into R and R_c bands, (iii) a substantially lower amount of free volume, and (iv) a slight reduction in the average free volume size. Furthermore, the spontaneous hydration layer on the two surfaces is studied, and its effect on the free volume is discussed. These results provide new insight into the soda lime silicate glass structure and have various technological implications for processes like chemical tempering or phenomena like surface defects nucleation.

KEYWORDS

Boson peak, Float glass, Free volume, Medium range order, Positron annihilation spectroscopy, Raman spectroscopy, Soda lime silcate glass

1 | INTRODUCTION

Inorganic glasses based on silica play a crucial role in various industries, including food and beverage, telecommunications, construction, and pharmaceuticals. Among the various manufacturing techniques, the most common method for producing glass sheets is the "float process," where a molten glass ribbon floats on the surface of a liquid tin bath upon cooling to achieve the desired thickness and width. As a result, commercial glass sheets exhibit physical and chemical asymmetry due to different thermal histories between the top and bottom surfaces and tin diffusion

into the glass network for several microns,[1–3] with a pronounced concentration gradient detectable within the first 100 nm beneath the surface.[4] This allows for the identification of the "tin side" (TS) and "air side" (AS) of the float glass. While the surface contacting the atmosphere is generally referred to as the "air side," it is worth emphasizing that float furnaces typically use a mixed N2–H2 environment to prevent massive oxidation of the molten tin bath. The typical temperatures at which the glass enters and exits the molten tin bath are about 1100°C and 600°C.[5]

This asymmetry affects several material properties, including the probability of crack nucleation under Vickers indentation,[6] the reactivity of the glass with water,[6] the crack propagation behavior,[7] the ion exchange kinetics during chemical tempering,[8,9] the refractive index of the surface,[10] the coloration acquired during ion exchange with silver ions,[11,12] the nanomechanical properties of the surface,[13,14] the glass transition temperature (*Tg*) and viscosity,[15] the adhesion with organic adhesives,[16] and the wear resistance.[17]

Although extensive research has explored the properties of both sides of float glass, little is known about the structural modifications induced by tin diffusion. Krohn et al.[15] demonstrated that replacing a small amount of modifier ions with Sn increases network connectivity, with a more pronounced effect when Sn^{4+} is present rather than Sn^{2+}. Surprisingly, no reports have systematically examined the structural differences between the AS and TS through the short (coordination of Si) and medium range (free volumes, ring structures, and correlation distances).

The identification of the ring nature in silicates is challenging. Raman spectroscopy is one of the most effective methods for detecting polymerized Si–O–Si rings, particularly in the 200–600 cm^{-1} wavenumber range, where ring breathing vibrations occur.[18] While Raman spectroscopy is highly sensitive to three- and four-membered rings (sometimes referred to as D_2 and D_1 bands), the response from larger structures is broad and overlapping, complicating their identification. On the other hand, Raman spectroscopy provides a deep insight into the short-range and the coordination environment of the Si-O tetrahedra, allowing a differentiation between bridging and non-bridging oxygens.

Synchrotron neutron diffraction offers a more powerful approach to determine ring sizes by identifying the first sharp diffraction peak (FSDP) associated with "ring spacing". In silicate glasses, the typical d-spacing associated with FSDP ranges from 3.0 Å to 4.5 Å,[19,20] this being associated with small-sized rings ($n < 6$–7).[20] Neutron diffraction is actually sensitive to the medium-range order on the few angstrom scale and starts to lose sensitivity on a longer scale ($n > 7$–8).[20] Molecular dynamics (MD) simulations have, however, spotted that larger rings can exist in amorphous silica with substantial ring populations up to $n = 10$.[21] The same simulations have also shown that 6-fold and 7-fold rings account for more than 50% of the ring population in amorphous SiO_2 with a rather homogeneous distribution between the two. This is in contrast with neutron diffraction analysis, where the experimentally calculated population of the 7-membered rings is about 1/5 of the 6-membered ones, and n larger than 8 is substantially not detected.[20] In addition, depolymerized silicate networks—like in commercial soda lime glass—could contain much larger rings with up to 30 members[22] (One shall remind that, in such a case, the free volume is not on the few nanometers scale as it is partially filled by the alkali cations bonded to the non-bridging oxygens). A second limitation of neutron diffraction resides in the fact that it probes a large volume of material, which makes it unsuitable for investigating changes in the glass structure located in a micrometric-sized region (i.e., the tin or air side).

Positron annihilation spectroscopy (PAS)[23–25] offers a valuable alternative to investigate the surface of silicate materials and provides a comprehensive understanding of their structure, being more sensitive to the large free volumes not detectable in disordered systems, by neutron diffraction. As an example, the positron annihilation lifetime spectra (PALS) of amorphous SiO_2 are typically characterized by three lifetimes.[26–28] The first one is associated with bulk annihilation overlapping with the para-positronium (p-Ps) annihilation at 125 ps; the second ranging from about 0.36 ns to 0.73 ns is related to the annihilation in vacancy sites and small voids (≈ 2.2 Å), respectively; the third is by far the most intense and it is related to a long lifetime of about 1.6 ns, corresponding to the ortho-positronium (o-Ps) annihilation in voids with an average size of about 4.9 Å.[28] We should remember that PALS probes the void size and not the Si–Si distance on the opposite side of the ring due to the electron cloud shielding. For amorphous silica at different densification levels under hydrostatic pressure, the shielding distance was calculated by comparing diffraction and PALS and resulted in about 0.6 Å. As such, we can infer that the main ring population in SiO_2 is about 5.5 Å. Such a value well matches relatively large 6–8-fold rings in relatively good agreement with the MD simulations.[21] As an example, 6-fold rings are in the order of 4.5 Å as detected by the FSDP.[19]

The present work aims to provide a deep investigation of the structure and chemistry differences between the air and tin side of soda lime silicate float glass, focusing on the short and medium-range order.

2 | MATERIALS AND METHODS

Commercial soda lime silicate float glass sheet with a nominal thickness of 4 mm was used in the present activity. The composition is (wt%): SiO_2 71.4%, Al_2O_3 1.0%, Na_2O 13.9%, K_2O 0.3%, MgO 4.1%, CaO 9.1%, and other 0.2%. Square samples of about 1.5 × 1.5 cm^2 were obtained with a diamond cutter. The glass was then cleaned with acetone in an ultrasonic bath (10 min).

The chemistry of the glass surface was assessed by secondary ion mass spectrometry (SIMS). The measurements were carried out with a dynamic SIMS Cameca SC-Ultra. Cs^+ primary ions were used as a sputtering beam at 3 KeV of impact energy, 62° incidence angle and 110 nA for a high sputtering rate. The acquired secondary ion species were positive MCs^+ molecular ions, where M indicates each element of interest. All SIMS depth profiles were normalized point by point to the signal of the sputtered Cs^+ secondary ions. This normalization method can correct any variations in the secondary ion yields occurring when the matrices are changing, like for TS and AS of the glass. Possible drifts in the secondary ion intensities induced by the charging effects occurring on dielectric samples can also be adjusted after normalization to Cs^+. A thin gold conductive capping layer was deposited on the sample surface before the SIMS measurements. This layer, with the aid of electron flooding, was mandatory in order to remove the excess of positive electric charge generated by the ion sputtering. The raster size was 200 × 200 μm^2, and the analyzed area for the secondary ions acquisition was centered within 66 × 66 μm^2 to avoid crater edge effects. The crater edge artifacts, generated by the contribution of secondary ions sputtered near the SIMS crater borders, i.e., from depths far from the measured crater bottom, reduce the depth resolution, and they get worse by increasing crater depth. They are certainly present for depth scales exceeding 10 μm, as in Figure 1. The impact of the crater edge effects on the depth resolution of the presented SIMS profiles can be neglected, considering the bulk nature of the samples. The depth scale was calibrated with the measurement of the final sputtered craters, by using a mechanical profilometer Tencor P6.

Variable–Energy PALS measurements were carried out at the Monoenergetic Positron Source (MePS) beamline at the ELBE (Electron Linac for beams with high Brillance and low Emittance) at the Helmholtz-Zentrum Dresden–Rossendorf (HZDR).[29] Positron Lifetime spectra were acquired at positron implantation energies ranging from 1 to 16 keV. Positrons are implanted with a Makovian profile, and the implantation energy is related to the mean positron implantation depth through a semi-empirical formula.[30] The used implantation energies, considering a density of 2.5 g/cm^3, span a depth from about 16 nm to 1.35 μm.

The PALS spectrum $F(t)$ is the convolution of the resolution function $\mathcal{R}(t)$ of the instrument (beam and detector) with a sum of decaying exponential functions:

$$F\ (t) = \mathcal{R}\ (t) \otimes \sum_j \frac{I_j}{\tau_j} exp\left(-\frac{t}{\tau_j}\right) + BG \qquad (1)$$

where, I_j and τ_j are the intensity and the lifetime of the different annihilating states of the positron in the material, BG being a constant background.

The details on detection and acquisition data are reported in previous works.[31,32] The lifetime spectra were deconvoluted by *PALfit* program[33] to extract the intensities and the lifetimes. All the fits had a reduced chi-square of around 1.0.

Lifetimes $\tau > 0.5$ ns are associated with the formation of o-Ps (lifetime of 142 ns in vacuum) whose lifetime is shortened by pick-off annihilations. In the pick-off process, a positron annihilates with an electron with the opposite spin of the void's wall, in which oPs is formed and trapped. There is an inverse relationship between the lifetime and size of the voids: the longer the lifetime larger the size of the voids. The void dimension can be evaluated by the quantum Tao-Eldrup equation.[34]

Raman spectra were collected using a Horiba-Jobin Yvon T-64000 triple-axis spectrometer in a double subtractive configuration. The system was equipped with three 1800 lines/mm holographic gratings and operated in back-scattering geometry. A liquid nitrogen-cooled charge-coupled device (CCD) detector (1024 × 256 pixels) provided a spectral resolution of approximately 0.6 cm^{-1} per pixel. The excitation source was a Cobolt Fandango 04-DPL solid-state laser (λ = 514.4 nm, 50 mW), with the laser power at the sample surface set to 10 mW. Low-frequency spectra were recorded in crossed polarization (HV). The analysis of low-frequency Raman spectra was performed according to the procedure outlined by Reference [35], taking into account the observed intensity (I^{obs}), which is proportional to the density of states g(ω). For a Stokes process, the frequency dependence of I^{obs} can be expressed as:

$$I^{obs}(\omega) = C(\omega)g(\omega)\frac{[n(\omega,T)+1]}{\omega} \qquad (2)$$

where, $C(\omega)$ represents the coupling function between light and vibration, which is approximated as $\sim\ \omega$ in the Boson peak (BP) range. By dividing the I^{obs} by $[n(\omega,T) + 1]$ (where $n(\omega,T)$ represents the Bose-Einstein factor) and ω, the reduced Raman intensity $I^{red}(\omega)$ can be written as:

$$I^{red}(\omega) = C(\omega)\frac{g(\omega)}{\omega^2} \qquad (3)$$

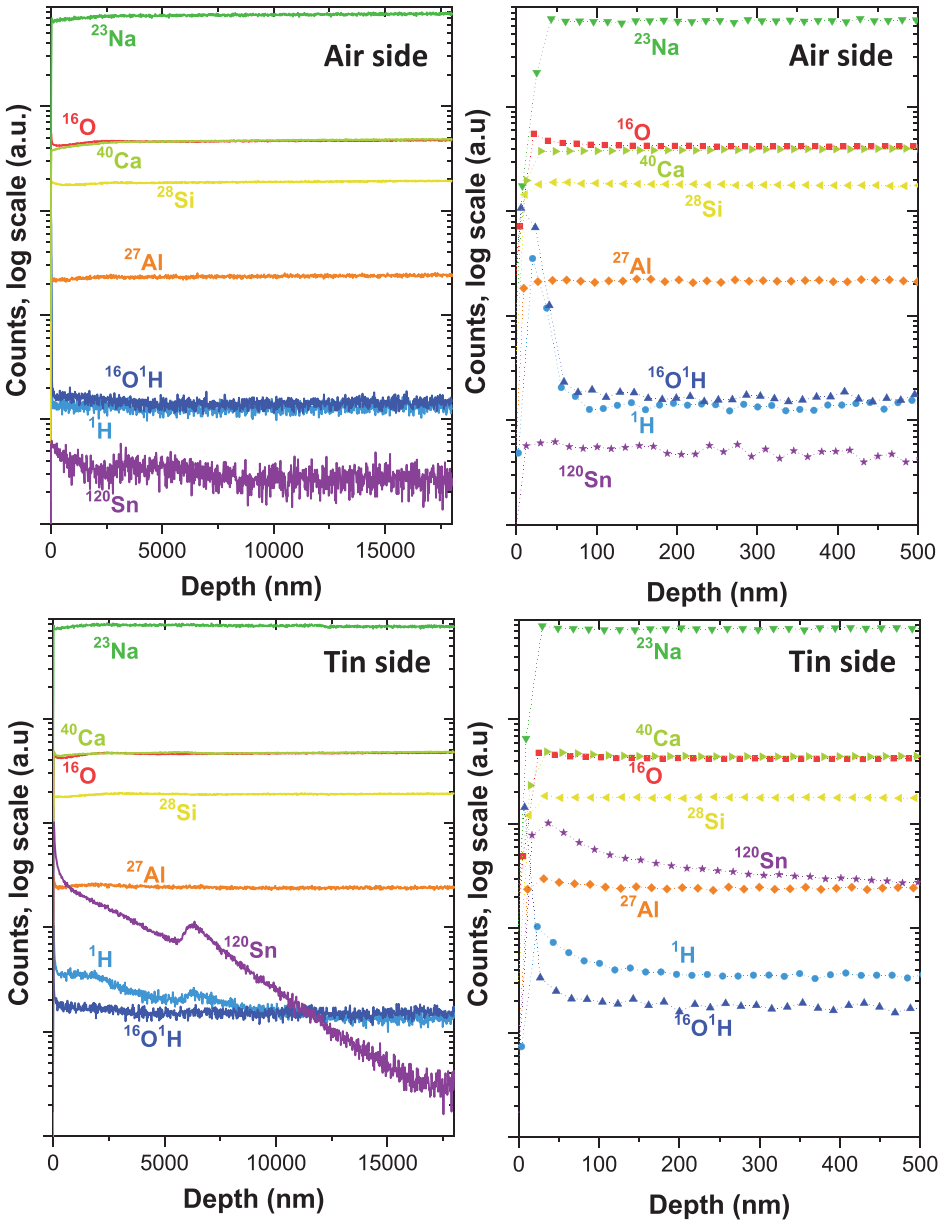

FIGURE 1 Secondary ion mass spectrometry (SIMS) counts as a function of depth for different ionic species on the AS and TS of commercial float glass.

The BP position (ω_{BP}) was determined by fitting the experimental data using a log-normal function according to Reference [36].

3 | RESULTS

A substantial inclusion of $^{16}O^{1}H$ and ^{1}H close to the surface of the air and tin side of the float glass can be detected by SIMS (Figure 1). This correlates with the presence of a surface hydrated layer, which is thicker on the air side (> 50 nm) than on the tin side (≈20 nm). The ^{120}Sn profile confirms the diffusion from the molten tin bath within the glass structure, and a strong peak in the Sn concentration can be observed at a depth of about 6.3 μm beneath the TS. This anomaly has already been reported and generally correlated with a change in the Sn oxidation state from 2+ (surface) to 4+ (bulk).[3]

The ratio between the SIMS counts for different ions and their respective counts in the "bulk" (averaged between 17.5 and 19 μm) is reported in Figure 2. One can observe that:

i. Besides the said highly hydrated layer on the surface, the $^{16}O^{1}H$ counts decrease smoothly down to about 4 μm, thus signaling the presence of water or OH

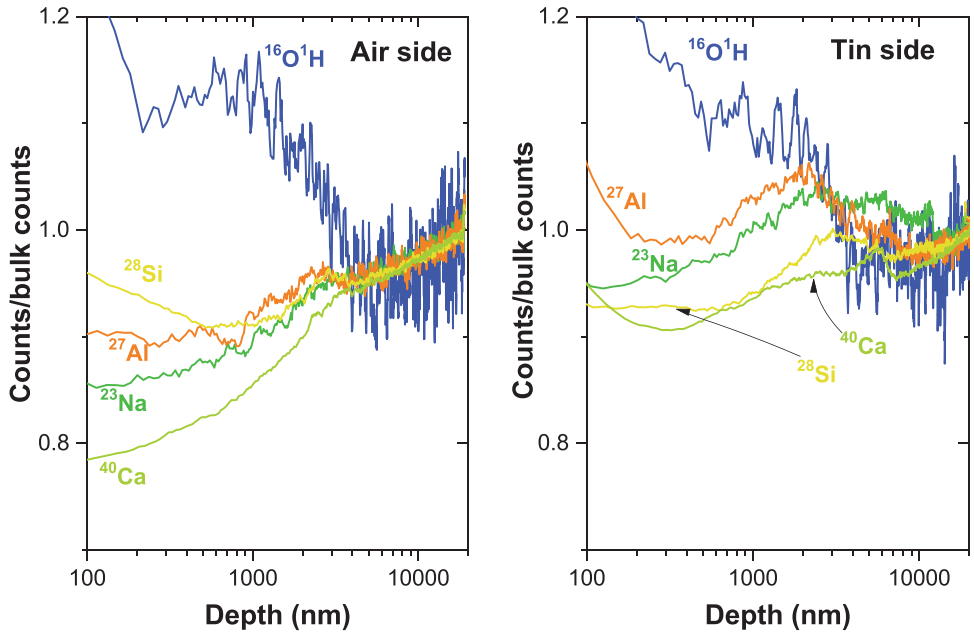

FIGURE 2 Secondary ion mass spectrometry (SIMS) counts ratio for different ionic species normalized to the counts in the bulk (17.5–19 μm) on the AS and TS of commercial float glass as a function of the erosion depth.

groups above the average value in the bulk. Generally thicker on the air side, this region is further characterized by a small but well-detectable gradient in the elemental composition of ^{28}Si, ^{27}Al, ^{23}Na, and ^{40}Ca.

ii. The SIMS counts for network modifiers like Na and Ca, decrease more than those for Si (former) and Al (intermediate) in the first micrometer beneath the surface on the air side. The tin side shows mixed results in the first micron: the Si data points lie between those for Ca and Na, while the amount of Al is slightly enhanced.

iii. A small but detectable signal from ^{120}Sn is visible also on the air side.

The PALS spectra as a function of the positron implantation energy (1–16 keV) reveal a clear evolution of the glass structure beneath the surface (Figure 3). The shape of the spectra strongly evolves up to 3–5 keV, with smaller changes occurring at higher positron implantation energies. The spectra can be deconvoluted using 3 lifetimes (Figure 4A,B). The most intense one (τ_2) is related to the direct e^+—e^- annihilation in the bulk or small cavities falling below the threshold for the positronium formation. Such a lifetime is in the order of 0.4 ns and is relatively stable regardless of the positron implantation energy or the side of the float glass under examination. The other two lifetimes originate from positronium-related annihilation events: τ_1 has been fixed at 0.125 ns to model the formation of p-Ps, while τ_3, coming from pick-off o-Ps annihilations, resulted in about 0.85–1.05 ns. The latter is associated with free volumes with size in the order of about 3 Å (Figure 4C).

The substantial differences between the air and tin sides can be spotted by the PALS spectra and their deconvolution (Figure 4). In general, the τ_3 associated with the o-Ps annihilation events is slightly longer on the AS than on the TS, reflecting larger free volumes (Figure 4C). While differences in the free volume size are relatively modest (≈10%), the changes in the intensities are substantial. In particular, we can spot that I_3 on the TS is smaller than on the AS. The relative differences in terms of I_3 range from about 20% in the "bulk" (16 keV of positron implantation energy) to more than 80% on the surface. As the positron implantation energy increases (i.e., the probed depth increases), the lifetimes and their intensities for the TS tend to approach those of the air side, without, however, reaching the same values at 16 keV (about 1.35 μm).

In addition to the substantial absence of tin diffusion on the air side, some evolution of the positron lifetimes and their intensities can still be detected as a function of the implantation energy. The free volume of the AS surface is larger (longer τ_3), and its concentration (smaller I_3) is lower than in the bulk. A similar effect can be seen on the tin side, though it seems more localized and detectable only when using 1 keV of positron implantation energy (c.a. 20–30 nm in depth). This mimics the trend observed in the positron annihilation Doppler broadening spectroscopy (DBS) reported in previous work on the same glass.[6] Note that the intensity I_3 on the TS surface is extremely weak, reducing the resolution in the determination of τ_3; for this reason, the data points on the

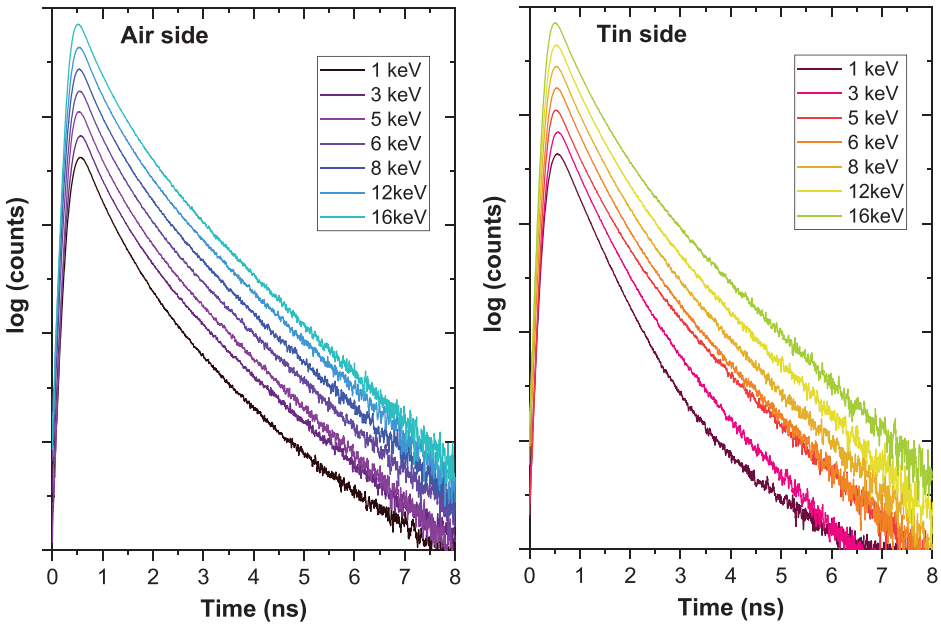

FIGURE 3 Positron annihilation lifetime spectra (PALS) obtained at different positron implantation energies on the air side and tin side of commercial float glass.

TS collected at 1 keV of positron implantation energy are drawn in faint red color.

The Q^n (n being the number of bridging oxygens coordinating silicon in a tetrahedral environment) region of the Raman spectra in Figure 5 shows a modest evolution as a function of depth on the tin side, while some differences can be noticed on the air side. Specifically, the low-frequency shoulder of the Q^n peak is weaker on the surface vicinity of the air side. The R region (Figure 5), including the breathing of 5+ rings, is characterized by modest evolution on the AS and TS and, in both cases, no clear evidence of the D_1 and D_2 bands (3 and 4-fold rings) can be detected.[37] The broad R feature is attributed to a dispersion in the Si–O–Si bonding angle in large rings, similar to what is usually observed in pure silica network.[37] On the other hand, an evolution of the R_c component (characteristic of alkali-containing glasses) can be observed, R_c being definitively weaker on the tin side surface. Although iron was not previously discussed in the text, we note that its concentration in this composition is below 0.2 wt%. Therefore, even though iron can display a Raman feature in the 950–990 cm^1 region that is sensitive to its oxidation state,[38,39] its spectral contribution is expected to be marginal.

The low-frequency portion of the Raman spectra is reported in Figure 6 for the bulk, the air side, and the tin side. The Boson Peak (BP, characteristic of amorphous structures, can be observed in all the different portions of the SLS, though its position and intensity vary. Specifically, it shifts to lower wavenumbers when moving from the bulk to AS and TS.

4 | DISCUSSION

The combination of Raman spectroscopy, PALS, and SIMS provides a comprehensive insight into the chemical and structural differences between the AS and TS of SLS float glass, as well as between the glass surface and its bulk.

The results show that some elemental depletion can be observed in the surface down to about 3–4 μm. As such, the relative ratios between the various metals (Si, Ca, Na, and Al) can vary up to 20% on the air side and up to about 10% on the tin side (Figure 2). Such chemical differences have various implications both on the scientific and technological level, the surface state of the glass being important in the ion exchange processes, chemical tempering, the resistance to corrosion and crack nucleation.

The first micrometer beneath the AS is glass-modifier-depleted (Na and Ca, Figure 2), leading to a slightly more polymerized network. While the Raman spectra (Figure 5) are relatively similar at different depths, we can recognize a small change in the Q^n region. A major band always dominates such a region at about 1090 cm^{-1}, which can be attributed to Q^3; however, the spectrum collected in the first micrometer beneath the AS is characterized by a weaker scattered intensity between 920 and 1100 cm^{-1}. It reflects the Q^1 and Q^2 units typically located in silicates at about 950 and 990 cm^{-1} (inset in Figure 5).[41] Hence, the Raman spectra provide evidence of a more polymerized structure in the air side vicinity, which is consistent with the chemical composition (Figure 2).

Chemistry evolution is less evident on the tin side, where the relative amount of modifiers (Na and Ca) and

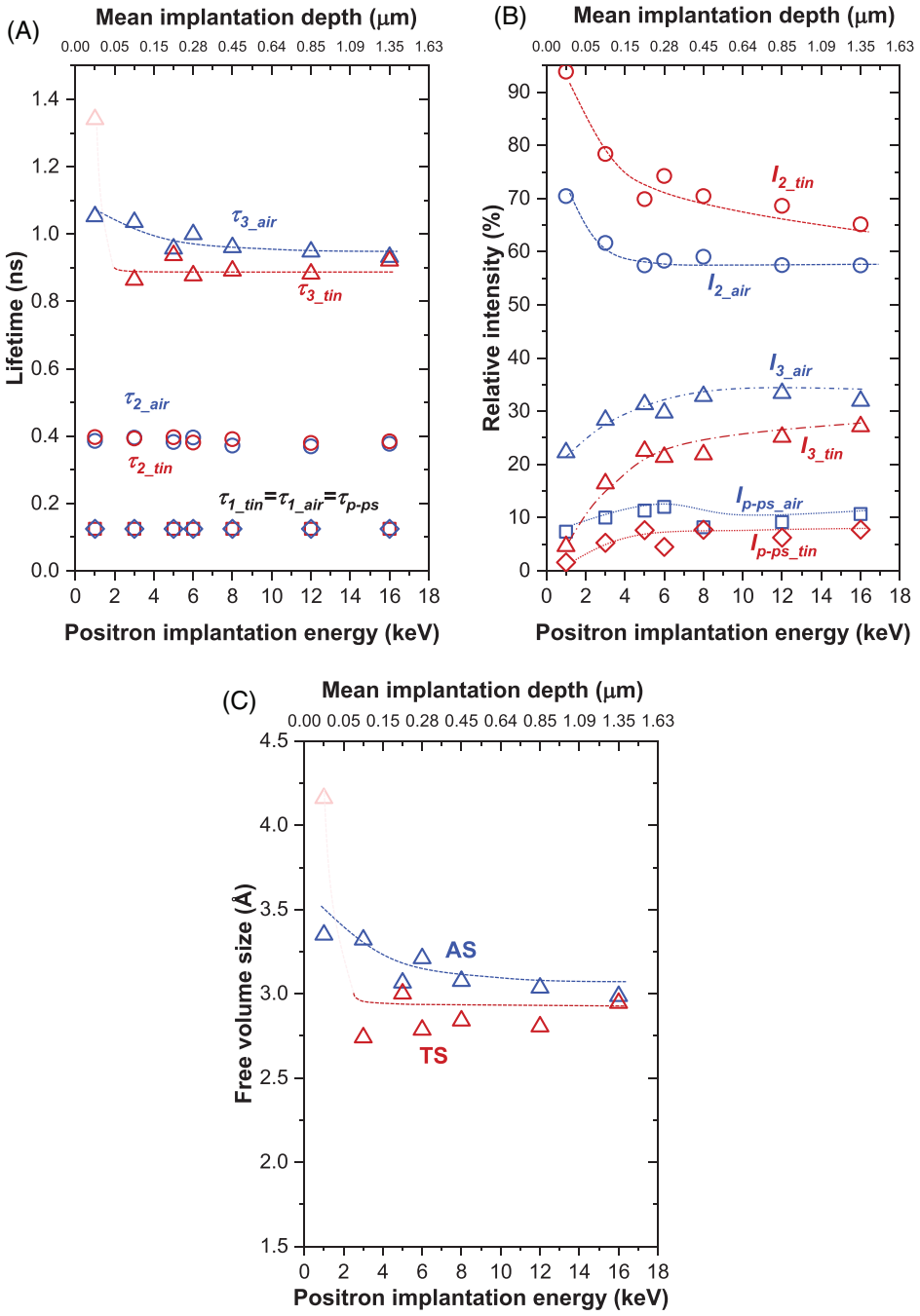

FIGURE 4 Deconvoluted (A) lifetimes and (B) intensities from the positron annihilation lifetime spectra (PALS) in Figure 3 as a function of the positron implantation energy (depth) for the AS and TS of SLS glass. (C) Average free volume size as calculated from the o-ps lifetime (τ_3) using Equation 1. Given the low intensity (I_3) associated with the τ_3 on the tin side surface (1 keV), the resolution in terms of lifetime and free volume size is reduced and, therefore, the datapoint is plotted in light red color. Red and blue datapoints refer to the air and tin side, respectively.

formers/intermediates (Si and Al) changes in a mixed way: the Si datapoints lie between Ca and Na, while there is a slight enrichment in Al. The relative abundance of Al increases the network connectivity as Al^{3+} in tetrahedral coordination causes the formation of negative charge centers, charge-balancing the "interstitial" positive modifiers without the formation of non-bridging oxygen (NBO). On the other hand, the TS surface is known to be enriched in Sn^{2+} till the hump[42] in the SIMS profile (about 6 μm beneath the surface, Figure 1). The impact of SnO on the glass structure has been debated; it can primarily act as a network modifier[43] but its incorporation increases the connectivity of the structure compared to alkalis and alkaline earth.[15] SnO could even act as an intermediate

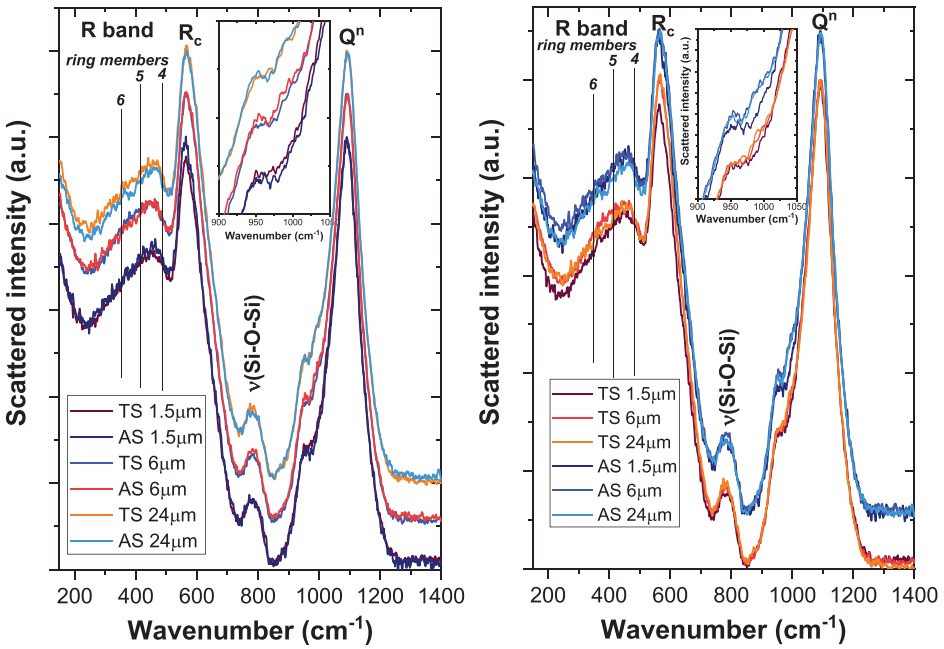

FIGURE 5 Medium and high-frequency regions of the Raman spectra collected on the air and tin side of SLS at different depths. The left panel evidences the differences between the AS and TS, while the right panel points out the spectra evolution with the position. The depths have been corrected using a refractive index of approximately 1.5, following the refraction model described by Reference [40].

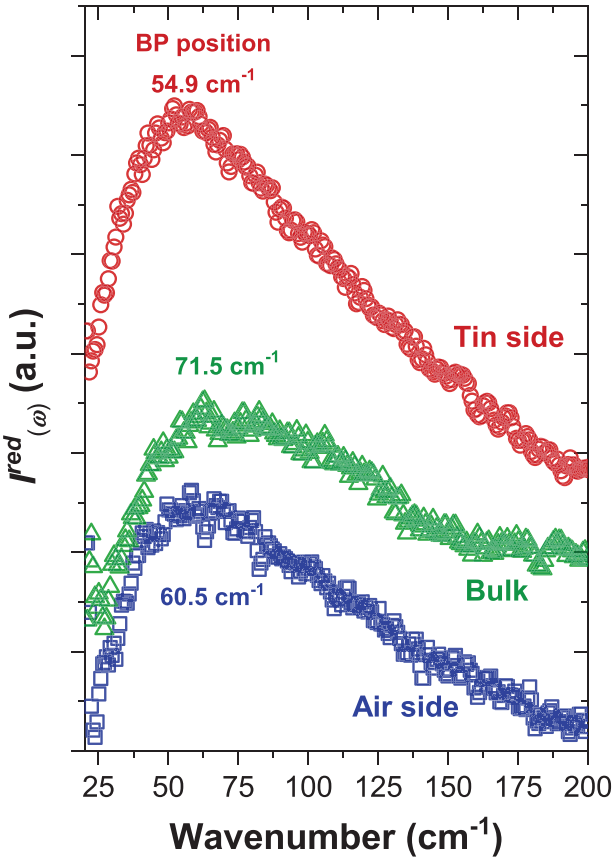

FIGURE 6 Low-frequency Raman spectra evidencing the boson peak region.

if the concentrations are high enough.[15,44] These mixed results in terms of relative concentration between modifiers and intermediates/formers cause a more stable Raman response in the Q^n region as a function of depth on the tin side (Figure 5). In summary, besides the clear tin incorporation, the short-range structure of the TS is akin to that of the bulk, much more so than that of the AS.

While the short range of the TS is surprisingly similar to the bulk, the medium range shows a different behavior. This can be evidenced on three distinctive levels: (i) the medium-frequency part of the Raman spectra (Figure 5), (ii) the low-frequency region of the Raman spectra and related BP position (Figure 6); (iii) the Positron annihilation spectra and related deconvolution parameters (Figures 3 and 4).

4.1 | Medium frequency Raman

The R_c Raman peak shows a certain evolution on the tin side (Figure 5), its intensity decreasing with the distance. R_c is a relatively sharp feature, generally attributed to localized vibrational modes (like structures that are vibrationally isolated from the network).[37,45] Such decoupling is thought to take place through the formation of segregated NBO structures that isolate some regions of the glass from the rest of the network. This causes a kind of "phase separation" at the nanoscale between silica-like (responsible for the broad R band) and alkali-silicate-like regions

(responsible for the sharp R_c band)[37] which can be organized in percolative nanoscopic channels.[46] The reduction of the R_c intensity on the tin side suggests that this "phase separation" in structurally different nano-domains is less developed as a result of tin incorporation. This argument is coherent with the fact that the splitting between R and R_c is generally less evident in alkali silicates containing heavy elements[37,45] as the steric hindrance of large modifiers does not allow the structure to relax as it wishes.[37] As the ionic radius for Sn^{2+} is about 122 pm,[47] much larger than that of Na^+ (≈102 pm),[48] its presence on the TS can reduce the intensity of R_c by suppressing the "phase separation".

4.2 | Low-frequency Raman

The low-frequency Raman spectra, dominated by the excess of vibrational states usually called Boson peak, show a detectable evolution on the glass surface vicinity. The BP position (ω_{BP}) is related to the characteristic size of elastic heterogeneities in the network and can be associated with the correlation length (ξ)[49,50] as:

$$\xi = \upsilon_t \, \omega_{BP}^{-1} \tag{4}$$

where, υ_t is the transverse sound velocity, which can be calculated from the shear modulus and the density. From the shear modulus measured by the acoustic resonance method and using a density of 2.5 g cm^3, one can estimate ξ as 1.8 nm in the bulk. We obtained the "true" ω_{BP} by correcting for the thermal effect as described in Reference [51] thereby determining its position in g (ω/ω^2). Such a value is in good agreement with the literature (1.8–2.2 nm in Reference [52]).

The decrease of ω_{BP} on the surface vicinity (Figure 6) is expected to mirror an increase in the correlation distance. Assuming that the elastic properties do not change and updating the density value considering the decrease in the free volume (calculated by averaging the I_3 data in Figure 4), and assuming that the total free volume of SLS is about 6%[53] in the bulk, one can estimate a correlation distance of about 2.2 and 2.5 on the AS and TS, respectively. There is indeed a relatively large uncertainty in these calculations related to the variation of the elastic properties and the density; however, the changes are substantial and deserve some comments. The first is related to the fact that ξ is longer on the AS than in the bulk. This is coherent with the observed local alkali depletion (Figure 2), actually, silica and aluminum-silicate glasses possess correlation distances larger than 3.3 nm.[49] The ξ increase moving from the bulk to the AS can be, therefore, attributed to a transition from the standard SLS composition to a more silica-rich network. On the other hand, the differences in ξ are even stronger on the TS where the network connectivity is quite similar to the bulk (see the Q^n region in Figure 5). Specifically, the correlation distance on the TS is substantially larger than on the bulk and (likely) AS. This can be tentatively ascribed to a more homogeneous and less "phase separated" network as a result of the steric hindrance to the network re-organization by the large Sn^{2+}. This further corroborates the lower R_c band intensity (Figure 5) on the TS, which is a signature of a more homogeneous structure.

4.3 | Positron annihilation lifetime spectroscopy

Both the AS and TS are characterized by PALS spectra clearly different from those of amorphous silica reported in the literature. The first feature is the absence, in SLS, of the long lifetime of 1.6 ns, which was dominant in SiO_2. Moreover, o-Ps in SLS accounts only for ≈ 30% of the total annihilation events (I_3), well below the typical values in SiO_2 (> 70%). The results point out that the SLS possess not only a smaller amount of free volume compared to SiO_2, a well-established argument coherent with the larger density of SLS (2.5 g cm^{-3} for SLS vs. 2.2 g cm^{-3} for SiO_2) but that the alkali and alkaline earth cations preferentially sits in the larger rings, i.e., those responsible for the 1.6 ns lifetime in silica, which cannot be detected in SLS.

When comparing the two faces of the float SLS, one can notice that the Sn diffusion substantially increases the density of the network, reducing the intensity I_3 associated with the o-Ps annihilation. While the effect is substantial in terms of intensity, it is definitely less remarkable in terms of free volume size, which is only marginally reduced on the TS (both AS and TS possess free volumes in the order of 3 Å with differences below 10%). In summary, the tin diffusion inside SLS glass during the manufacturing process causes densification of the structure with tin, therefore, likely filling interstitial voids, and acts as a glass modifier. These results are consistent with the fact that the tin side possesses substantially different properties, including a higher probability of crack formation after Vickers indentation and lower kinetics of the ion exchange process.[6,8,9] Actually, the nucleation of cracks is facilitated in highly packed glasses, which do not possess the ability to densify during indentation, relaxing the mechanical stresses.[54] Besides ion exchange and the mechanical properties, the chemical durability and weathering might be affected.[55] For instance, the water incorporation kinetics on the tin side in hydrothermal conditions are slower than on the air side.[6] This reflects on various properties, including the dynamic fatigue response.[56,57]

Finally, we can notice a strong evolution of PALS parameters on the surface vicinity (up to 3–4 keV on the air side and up to 2.5 keV on the tin side) both in terms of lifetimes and intensities (Figure 4). This mimics the $O^{16}H^2$ signal associated with water penetration (Figure 1). The surface is clearly denser with reduced I_3 (lower total void volume) also on the air side where the tin presence is modest. However, the size of the free volume is generally larger close to the surface (longer τ_3). Water has, therefore, a "singular" behavior: it causes densification of the glass surface (coherent with the fact that it is larger than the replaced Na^+) but simultaneously increases the "void" size. Such a phenomenon cannot be explained by a simple and rigid substitution of either Si-OH+H_2O or H_3O^+ for Na^+ but suggests the activation of some kind of rearrangement of the structural units even in ambient conditions.

5 | CONCLUSIONS

The air and tin sides of soda lime silicate float glass are substantially different in terms of chemistry, short-, and medium-range order. Surprisingly, the short-range (Q^n units and distribution of non-bridging oxygens) on the tin side is akin to that of the bulk despite the obvious diffusion of Sn within the glass structure, whereas larger differences can be identified on the air side. This is attributed to a chemical modification, depleting the modifiers in the first micrometer beneath the air side surface. This results in a more polymerized network on the AS.

On the other hand, the Sn intercalation causes a substantial change in the medium-range order of the TS. The tin side is denser than the air side with a marked reduction in the amount of free volume (reduction in the o-ps annihilation events). While the amount of free volume is substantially different, its size changes only marginally (variation of about 10%) and is always in the order of 3 Å. Furthermore, the typical splitting of the medium-frequency portion of the Raman spectra in $R + R_c$ band is slightly less developed on the tin side, highlighting a more homogeneous network with reduced segregation of alkalis/non-bridging oxygens. Such observation matches with a detectable decrease in the Boson peak frequency (longer correlation distances) on the tin side.

Differences in the spontaneous surface hydration layer thickness can also be pointed out on the two sides of the glass, substantially reducing the amount of free volume in the first tens of nanometers close to the glass surface.

ACKNOWLEDGMENTS

The beamtime at HZRD was supported by the projects TemPoS and HydroGlass. Parts of this research were carried out at ELBE at the Helmholtz-Zentrum Dresden—Rossendorf e. V., a member of the Helmholtz Association. We would like to thank the facility staff for their assistance.

The authors would like to thank the Centre for Technological Platforms (CPT) of the University of Verona (Italy) for providing access to scientific instrumentation and technical support.

ORCID

Mattia Biesuz https://orcid.org/0000-0002-4338-4177
Levent Karacasulu https://orcid.org/0000-0003-4710-2816
Michele Cassetta https://orcid.org/0000-0003-2078-655X
Mario Barozzi https://orcid.org/0000-0002-1308-4261
Roberto Canteri https://orcid.org/0000-0002-0895-8884
Maciej Oskar Liedke https://orcid.org/0000-0001-7933-7295
Eric Hirschmann https://orcid.org/0000-0001-5782-9627
Andreas Wagner https://orcid.org/0000-0001-7575-3961
Sebastiano Mariazzi https://orcid.org/0000-0001-9985-8792
Gian D. Sorarù https://orcid.org/0000-0002-0453-3379
Vincenzo M. Sglavo https://orcid.org/0000-0001-9133-7204
Roberto S. Brusa https://orcid.org/0000-0002-5239-7172

REFERENCES

1. Townsend PD, Can N, Chandler PJ, Farmery BW, Lopez-Heredero R, Peto A, et al. Comparisons of tin depth profile analyses in float glass. J Non Cryst Solids. 1998;223(1–2):73–85. https://doi.org/10.1016/S0022-3093(97)00348-7
2. Yang B, Townsend PD, Holgate SA. Cathodoluminescence and depth profiles of tin in float glass. J Phys D Appl Phys. 1994;27(8):1757–62. https://doi.org/10.1088/0022-3727/27/8/026
3. Frischat GH. Tin ions in float glass cause anomalies. Comptes Rendus Chimie. 2002;5(11):759–63. https://doi.org/10.1016/S1631-0748(02)01436-4
4. Colombin L, Jelli A, Riga J, Pireaux JJ, Verbist J. Penetration depth of tin in float glass. J Non Cryst Solids. 1977;24(2):253–8. https://doi.org/10.1016/0022-3093(77)90048-5
5. Varshneya AK. Fundamentals of inorganic glasses. New York: Academic Press, Inc.; 1994 https://doi.org/10.1016/0022-3093(94)90112-0
6. Sorarù GD, Mariazzi S, Barozzi M, Canteri R, Cassetta M, Pellegrini D, et al. On the structure and properties of hydrothermally toughened soda–lime silicate float glass. J Am Ceram Soc. 2024;107(8):5383–99. https://doi.org/10.1111/jace.19832
7. Krohn M, Hellmann JR, Pantano CG, Lower N, Brow RK. Effects of tin on the physical properties and crack growth in soda-lime-silica float glass. Key Eng Mater. 2004;264–268:1859–62. https://doi.org/10.4028/www.scientific.net/KEM.264-268.1859
8. Jiang L, Guo X, Li X, Li L, Zhang G, Yan Y. Different K^+–Na^+ inter-diffusion kinetics between the air side and tin side of an ion-exchanged float aluminosilicate glass. Appl Surf

Sci. 2013;265:889–94. https://doi.org/10.1016/j.apsusc.2012.11.143

9. Li X, Jiang L, Wang Y, Mohagheghian I, Dear JP, Li L, et al. Correlation between K^+-Na^+ diffusion coefficient and flexural strength of chemically tempered aluminosilicate glass. J Non Cryst Solids. 2017;471:72–81. https://doi.org/10.1016/j.jnoncrysol.2017.05.011
10. Synowicki RA, Johs BD, Martin AC. Optical properties of soda-lime float glass from spectroscopic ellipsometry. Thin Solid Films. 2011;519(9):2907–13. https://doi.org/10.1016/j.tsf.2010.12.110
11. Biesuz M, Mariotto G, Cassetta M, Ersen O, Ihiawakrim D, Haušild P, et al. Solid-State field-assisted ion exchange (Ag → Na) in soda–Lime float glass: tin versus air side. Adv Eng Mater. 2023;25(18):2201572. https://doi.org/10.1002/adem.202201572
12. Mareska A. Formation of silver colloids on the tin side of the float glass. Ceramics—Silikaty. 2023;348–59. https://doi.org/10.13168/cs.2023.0035
13. Howell JA, Hellmann JR, Muhlstein CL. Nanomechanical properties of commercial float glass. J Non Cryst Solids. 2008;354(17):1891–9. https://doi.org/10.1016/j.jnoncrysol.2007.10.021
14. Goodman O, Derby B. The mechanical properties of float glass surfaces measured by nanoindentation and acoustic microscopy. Acta Mater. 2011;59(4):1790–9. https://doi.org/10.1016/j.actamat.2010.11.045
15. Krohn MH, Hellmann JR, Mahieu B, Pantano CG. Effect of tin-oxide on the physical properties of soda-lime–silica glass. J Non Cryst Solids. 2005;351(6–7):455–65. https://doi.org/10.1016/j.jnoncrysol.2005.01.050
16. Bornemann S, Henning S, Naumenko K, Pander M, Thavayogarajah N, Würkner M. Strength analysis of laminated glass/EVA interfaces: microstructure, peel force and energy of adhesion. Compos Struct. 2022;297:115940. https://doi.org/10.1016/j.compstruct.2022.115940
17. He H, Liu H, Lin Y, Qu C, Yu J, Kim SH. Differences in indentation and wear behaviors between the two sides of thermally tempered soda lime silica glass. J Am Ceram Soc. 2021;104(9):4718–27. https://doi.org/10.1111/jace.17872
18. De Leeuw SW, He H, Thorpe MF. Vibrational spectra of rings in vitreous silica. Solid State Commun. 1985;56(4):343–6. https://doi.org/10.1016/0038-1098(85)90398-9
19. Shi Y, Neuefeind J, Ma D, Page K, Lamberson LA, Smith NJ, et al. Ring size distribution in silicate glasses revealed by neutron scattering first sharp diffraction peak analysis. J Non Cryst Solids. 2019;516:71–81. https://doi.org/10.1016/j.jnoncrysol.2019.03.037
20. Zhou Q, Shi Y, Deng B, Neuefeind J, Bauchy M. Experimental method to quantify the ring size distribution in silicate glasses and simulation validation thereof. Sci Adv. 2021;7(28):eabh1761. https://doi.org/10.1126/sciadv.abh1761
21. Shiga M, Hirata A, Onodera Y, Masai H. Ring-originated anisotropy of local structural ordering in amorphous and crystalline silicon dioxide. Commun Mater. 2023;4(1):91. https://doi.org/10.1038/s43246-023-00416-w
22. Yuan X, Cormack AN. Efficient algorithm for primitive ring statistics in topological networks. Comput Mater Sci. 2002;24(3):343–60. https://doi.org/10.1016/S0927-0256(01)00256-7
23. Siegel RW. Positron annihilation spectroscopy. Ann Rev Mater Sci. 1980;10(1):393–425. https://doi.org/10.1146/annurev.ms.10.080180.002141
24. Egger W. Pulsed low-energy positron beams in materials sciences, in: physics with many positron. In: Dupasquier, A, Mills Jr. AP, Brusa, RS, editors. Proceedings of the International School of Physics "Enrico Fermi". 2010:419–49. https://doi.org/10.3254/978-1-60750-646-1-419
25. Dull TL, Frieze WE, Gidley DW, Sun JN, Yee AF. Determination of pore size in mesoporous thin films from the annihilation lifetime of positronium. J Phys Chem B. 2001;105(20):4657–62. https://doi.org/10.1021/jp004182v
26. Ravelli L, Macchi C, Mariazzi S, Mazzoldi P, Egger W, Hugenschmidt C, et al. Interstitial oxygen related defects and nanovoids in Au implanted a -SiO_2 glass depth profiled by positron annihilation spectroscopy. J Phys D Appl Phys. 2015;48(49):495302. https://doi.org/10.1088/0022-3727/48/49/495302
27. Inoue K, Kataoka H, Nagai Y, Hasegawa M, Kobayashi Y. Short and medium range order in two-component silica glasses by positron annihilation spectroscopy. J Appl Phys. 2014;115(20):204903. https://doi.org/10.1063/1.4878457
28. Zanatta M, Baldi G, Brusa R S, Egger W, Fontana A, Gilioli E, et al. Structural evolution and medium range order in permanently densified vitreous SiO_2. Phys Rev Lett. 2014;112(4):045501. https://doi.org/10.1103/PhysRevLett.112.045501
29. Wagner A, Butterling M, MO L, Potzger K, Krause-Rehberg R. Positron annihilation lifetime and doppler broadening spectroscopy at the ELBE facility. AIP Conf Proceed. 2018;1970:040003. https://doi.org/10.1063/1.5040215
30. Schultz PJ, Lynn KG. Interaction of positron beams with surfaces, thin films, and interfaces. Rev Mod Phys. 1988;60(3):701–79. https://doi.org/10.1103/RevModPhys.60.701
31. Magrin Maffei R, Butterling M, Liedke MO, D'Addato S, di Bona A, Bertoni G, et al. Defectivity of Al:ZnO thin films with different crystalline order probed by positron annihilation spectroscopy. Appl Surf Sci. 2024;665:160240. https://doi.org/10.1016/j.apsusc.2024.160240
32. Hirschmann E, Butterling M, Hernandez Acosta U, Liedke MO, Attallah AG, Petring P, et al. A new system for real-time data acquisition and pulse parameterization for digital positron annihilation lifetime spectrometers with high repetition rates. J Instrument. 2021;16(08):P08001. https://doi.org/10.1088/1748-0221/16/08/P08001
33. Olsen JV, Kirkegaard P, Pedersen NJ, Eldrup M. PALSfit: a new program for the evaluation of positron lifetime spectra. Physica status Solidi C. 2007;4(10):4004–6. https://doi.org/10.1002/pssc.200675868
34. Eldrup M, Lightbody D, Sherwood JN. The temperature dependence of positron lifetimes in solid pivalic acid. Chem Phys. 1981;63(1–2):51–8. https://doi.org/10.1016/0301-0104(81)80307-2
35. Shuker R, Gammon RW. Raman-scattering selection-rule breaking and the density of states in amorphous materials. Phys Rev Lett. 1970;25(4):222–5. https://doi.org/10.1103/PhysRevLett.25.222
36. Cassetta M. Medium-range structure modifications induced by Fe^{3+}/Fe_{tot}. in volcanic glasses: a low-frequency Raman spectroscopy study. Eur Phys J Plus. 2024;139(1):45. https://doi.org/10.1140/epjp/s13360-023-04838-w

37. Hehlen B, Neuville DR, Kilymis D, Ispas S. Bimodal distribution of Si–O–Si angles in sodo-silicate glasses. J Non Cryst Solids. 2017;469:39–44. https://doi.org/10.1016/j.jnoncrysol.2017.04.009
38. Magnien V, Neuville DR, Cormier L, Roux J, Hazemann J-L, Pinet O, et al. Kinetics of iron redox reactions in silicate liquids: A high-temperature X-ray absorption and Raman spectroscopy study. J Nucl Mater. 2006;352(1–3):190–5. https://doi.org/10.1016/j.jnucmat.2006.02.053
39. Cassetta M, De Bona E, Sambugaro A, Enrichi F, Daldosso N, Giannetta B, et al. Fe-dependent structural evolution of peralkaline soda aluminosilicate glasses: iron speciation vs. glass transition. Chem Geol. 2025;674:122561. https://doi.org/10.1016/j.chemgeo.2024.122561
40. Everall NJ. Modeling and measuring the effect of refraction on the depth resolution of confocal Raman microscopy. Appl Spectrosc. 2000;54(6):773–82. https://doi.org/10.1366/0003702001950382
41. Rahman A, Mariotto G, Cattaruzza E, Trave E, Gonella F, Quaranta A. Thermal annealing and laser induced structural rearrangement and silver state modification in Ag^{+}-Na^{+} ion-exchanged silicate glasses studied by Raman spectroscopy. J Non Cryst Solids. 2021;552:120455. https://doi.org/10.1016/j.jnoncrysol.2020.120455
42. Hayashi Y, Matsumoto K, Kudo M. The diffusion mechanism of tin into glass governed by redox reactions during the float process. J Non Cryst Solids. 2001;282(2–3):188–96. https://doi.org/10.1016/S0022-3093(01)00319-2
43. Suzuki K, Tricot G, Revel B, Saitoh A. Properties and structure of $SnO-SiO_2$ and $SnO-SnF_2-SiO_2$ glasses. J Non Cryst Solids. 2020;527:119706. https://doi.org/10.1016/j.jnoncrysol.2019.119706
44. Holland D, Smith ME, Poplett IJF, Johnson JA, Thomas MF, Bland J. Tin germanate glasses. J Non Cryst Solids. 2001;293–295:175–81. https://doi.org/10.1016/S0022-3093(01)00668-8
45. Matson DW, Sharma SK, Philpotts JA. The structure of high-silica alkali-silicate glasses. A Raman spectroscopic investigation. J Non Cryst Solids. 1983;58(2–3):323–52. https://doi.org/10.1016/0022-3093(83)90032-7
46. Le Losq C, Neuville DR, Chen W, et al. Percolation channels: A universal idea to describe the atomic structure and dynamics of glasses and melts. Sci Rep. 2017;7(1):16490. https://doi.org/10.1038/s41598-017-16741-3
47. Junio JB, Chirawatkul P, Conato MT, Mercado CC. Substitution of Ca^{2+} in calcite by Sn^{2+} and Sr^{2+} cations through ion exchange characterized by X-ray absorption and photoelectron spectroscopies. MRS Adv. 2021;6(12):342–9. https://doi.org/10.1557/s43580-021-00061-w
48. Chiang Y-M, Birnie D, Kingery PWD. Physical Ceramics: Principles for Ceramic Science and Engineering. New York: Wiley; 1997
49. Ando MF, Benzine O, Pan Z, Garden J-L, Wondraczek K, Grimm S, et al. Boson peak, heterogeneity and intermediate-range order in binary SiO2-Al2O3 glasses. Sci Rep. 2018;8(1):5394. https://doi.org/10.1038/s41598-018-23574-1
50. Cassetta M, Mariotto G, Daldosso N, De Bona E, Biesuz M, Sorarù GD, et al. Viscosity, boson peak and elastic moduli in the Na_2O-SiO_2 system. Minerals. 2023;13(9):1166. https://doi.org/10.3390/min13091166
51. Cassetta M, Szewczyk D, Giuliani G, Dominijanni S, Vetere F, Iezzi G, et al. Chemically driven nano-elastic heterogeneities control fragility in volcanic melts. Adv Sci. 2025;e12063. https://doi.org/10.1002/advs.202512063
52. Pan Z, Benzine O, Sawamura S, Limbach R, Koike A, Bennett TD, et al. Disorder classification of the vibrational spectra of modern glasses. Phys Rev B. 2021;104(13):134106. https://doi.org/10.1103/PhysRevB.104.134106
53. Rouxel T, Ji H, Hammouda T, Moréac A. Poisson's ratio and the densification of glass under high pressure. Phys Rev Lett. 2008;100(22):225501. https://doi.org/10.1103/PhysRevLett.100.225501
54. Rouxel T, Jang J, Ramamurty U. Indentation of glasses. Prog Mater Sci. 2021;121:100834. https://doi.org/10.1016/j.pmatsci.2021.100834
55. Justino de Lima C, Aldinger B, de Haan P, Bristogianni T, Veer F. Effects of composition on the durability and weathering of flat glass. Glass Struc Engg. 2022;7(2):139–55. https://doi.org/10.1007/s40940-022-00175-z
56. Tummala RR, Foster BJ. Strength and dynamic fatigue of float glass surfaces. J Am Ceram Soc. 1975;58(3–4):156–6. https://doi.org/10.1111/j.1151-2916.1975.tb19593.x
57. Krohn MH, Hellmann JR, Shelleman DL, Pantano CG, Sakoske GE. Biaxial flexure strength and dynamic fatigue of soda–lime–silica float glass. J Am Ceram Soc. 2002;85(7):1777–82. https://doi.org/10.1111/j.1151-2916.2002.tb00352.x

How to cite this article: Biesuz M, Karacasulu L, Cassetta M, Barozzi M, Canteri R, Liedke MO, et al. On the asymmetry of soda lime silicate float glass structure and chemistry. J Am Ceram Soc. 2026;109:e70488. https://doi.org/10.1111/jace.70488